ELSEVIER

Volume 180, Number 4, April 2007

JOURNAL OF SOLID STATE CHEMISTRY

www.elsevier.com/locate/jssc

CONTENTS

Abstracted/indexed in BioEngineering Abstracts, Chemical Abstracts, Coal Abstracts, Current Contents/Physics, Chemical, & Earth Sciences, Engineering Index, Research Alert, SCISEARCH, Science Abstracts, and Science Citation Index. Also covered in the abstract and citation database SCOPUS®. Full text available on ScienceDirect®.

Regular Articles

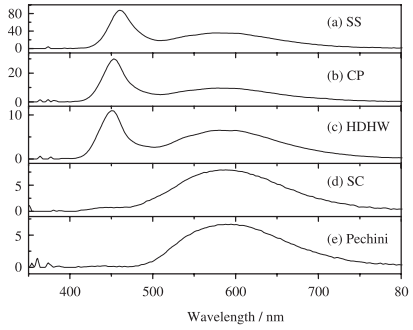

Emission spectra of the LEDs with TAG:$0.03Ce^{3+}$ phosphors synthesized by different methods (SS (a); CP (b); HDHW (c); SC (d); Pechini (e)) under 20 mA forward bias.

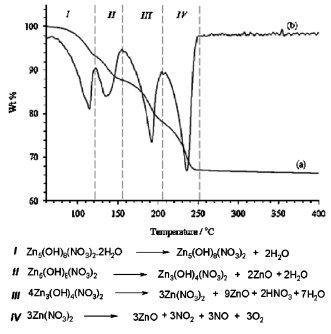

TG and DTG profiles for $Zn_5(OH)_8(NO_3)_2 \cdot 2H_2O$ and the corresponding reactions occurring at each step.

Regular Articles—Continued

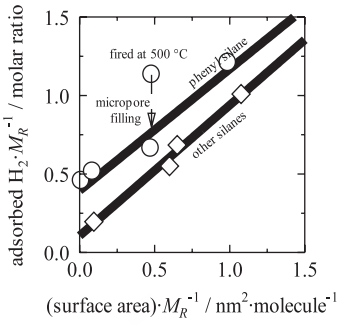

Dependence of amount of adsorbed H_2 per organic component on surface area per organic component. Their intercept and slope indicate strength of physicochemical interaction and physisorption. Phenyl groups modified on mesoporous silica show the stronger physicochemical interaction than other functional groups for H_2 adsorption.

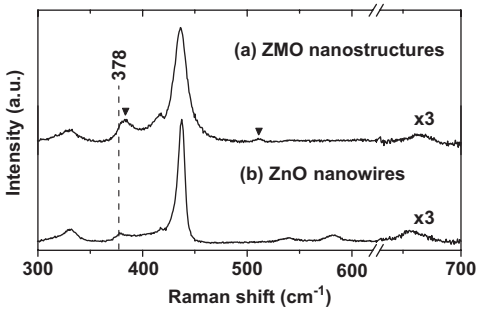

We reported the synthesis of the ZnMgO nanostructures prepared by a simple vapor transport method. Magnesium-related anomalous modes are observed by Raman spectra for the first time in ZnMgO system.

Structure and antiferroelectric properties of cesium niobate, $Cs_2Nb_4O_{11}$

Robert W. Smith, Chunhua Hu, Jianjun Liu, Wai-Ning Mei and Kuan-Jiuh Lin

Page 1193

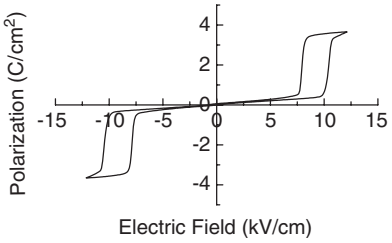

The crystal structure of $Cs_2Nb_4O_{11}$ is in the nonpolar point group *mmm* and centrosymmetric space group *Pnna*. This symmetry is consistent with antiferroelectric character, which the material exhibits, as shown by double hysteresis loops in the polarization versus electric-field plot.

Vibrational spectra and H-bondings in anhydrous and monohydrate α-Zr phosphates

Mario Casciola, Anna Donnadio, Francesca Montanari, Paolo Piaggio and Valeria Valentini

Page 1198

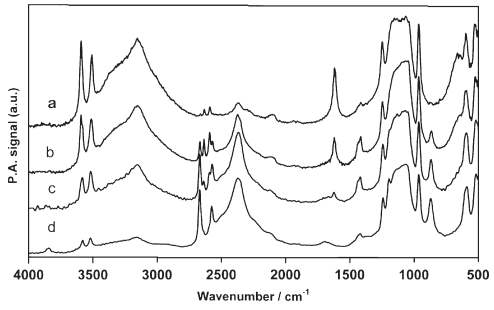

A detailed analysis of the vibrational spectra of α-zirconium phosphates allowed to obtain an affordable band assignment highlighting the hydrogen bonding structure formed by the P–OH groups and the intercalated water molecules, the dehydration mechanism and the changes in the interlayer region induced by the α to β phase transition.

Structural characterization, magnetic behavior and high-resolution EELS study of new perovskites $Sr_2Ru_{2-x}Co_xO_{6-\delta}$ ($0.5 \leqslant x \leqslant 1.5$)

A.D. Lozano-Gorrín, J.E. Greedan, P. Núñez, C. González-Silgo, G.A. Botton and G. Radtke

Page 1209

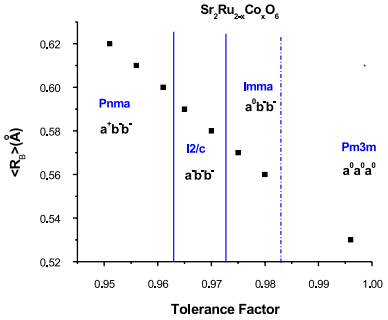

Correlation between the average *B*-site radius, the Goldschmidt tolerance factor and the sequence of space groups and Glazer tilt systems found for the perovskite solid solution $Sr_2Ru_{2-x}Co_xO_6$.

Formation of α-Mn_2O_3 nanorods via a hydrothermal-assisted cleavage-decomposition mechanism

Youcun Chen, Yuanguang Zhang, Qi-Zhi Yao, Gen-Tao Zhou, Shengquan Fu and Hai Fan

Page 1218

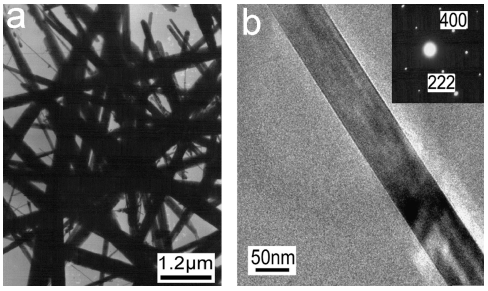

A hydrothermal cleavage-decomposition mechanism was used to synthesize single-crystal α-Mn_2O_3 nanorods at 160 °C for 16 h. These nanorods exhibit single-crystal nature, and have an average diameter of 36 nm and lengths of up to 1 μm.

Synthesis, crystal structure and mono-dimensional thallium ion conduction of $TlFe_{0.22}Al_{0.78}As_2O_7$

Najoua Ouerfelli, Abderrahmen Guesmi, Daniele Mazza, Adel Madani, Mohamed Faouzi Zid and Ahmed Driss

Page 1224

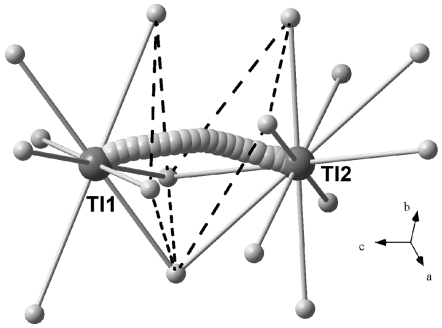

Optimized trajectory for Tl(1)–Tl(2) jump.

Synthesis and UV absorption properties of 5-sulfosalicylate-intercalated Zn–Al layered double hydroxides

Linyan Zhang, Yanjun Lin, Zhenjun Tuo, David G. Evans and Dianqing Li

Page 1230

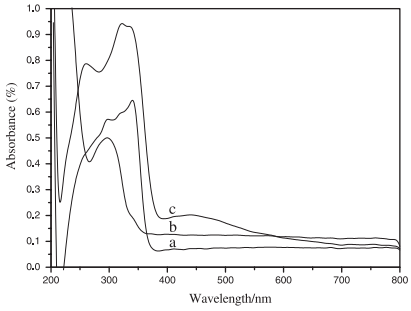

UV–visible absorbance curves of SSA (a), ZnAl–NO_3–LDHs precursor (b) and ZnAl–SSA–LDHs (c).

Continued

Syntheses of rare-earth metal oxide nanotubes by the sol–gel method assisted with porous anodic aluminum oxide templates

Qin Kuang, Zhi-Wei Lin, Wei Lian, Zhi-Yuan Jiang, Zhao-Xiong Xie, Rong-Bin Huang and Lan-Sun Zheng

Page 1236

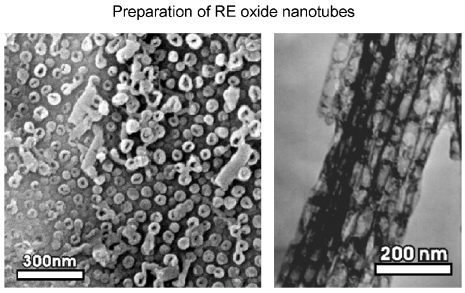

A versatile synthetic method for the preparation of ordered rare-earth (RE) oxide nanotubes is reported, by which RE (RE = Y, Ce, Pr, Nd, Sm, Eu, Gd, Tb, Dy, Ho, Er, Yb) oxide nanotubes were successfully prepared from corresponding RE nitrate solution via the sol–gel method assisted with porous anodic aluminum oxide (AAO) templates.

Structural evolution in iron tellurates

A. van der Lee and R. Astier

Page 1243

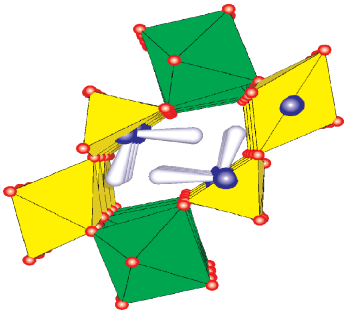

The structures of three new iron tellurates have been determined and compared with four other iron tellurates known from the literature. The Te^{4+} lone pairs tend to align in tunnels, such as in the structure of $Fe_3Te_4O_{12}$.

Phase transition and mixed oxide-proton conductivity in germanium oxy-apatites

Laura León-Reina, José M. Porras-Vázquez, Enrique R. Losilla and Miguel A.G. Aranda

Page 1250

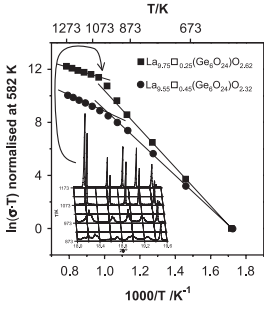

$La_{9.75}\square_{0.25}(Ge_6O_{24})O_{2.62}$ oxide-conductor shows triclinic–hexagonal phase transition (see inset) at ~1020 K, meanwhile $La_{9.55}\square_{0.45}(Ge_6O_{24})O_{2.32}$ is hexagonal at all temperatures. Both compounds have mixed proton and oxide conductivities below 600 K.

Ionic and electronic transport in $La_2Ti_2SiO_9$-based materials

Y.V. Pivak, V.V. Kharton, E.N. Naumovich, J.R. Frade and F.M.B. Marques

Page 1259

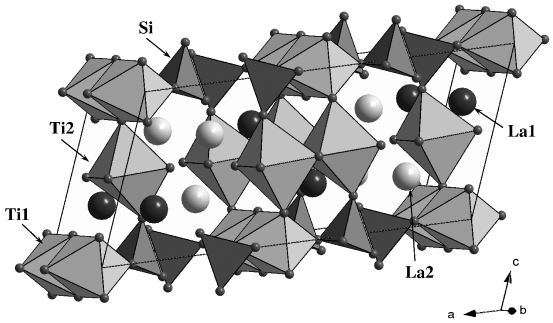

Structure of mixed-conducting $(La,Pr)_2(Ti,Nb)_2SiO_9$.

Synthesis of Fe_3O_4 particle-chain microwires in applied magnetic field

Fashen Li, Ying Wang and Tao Wang

Page 1272

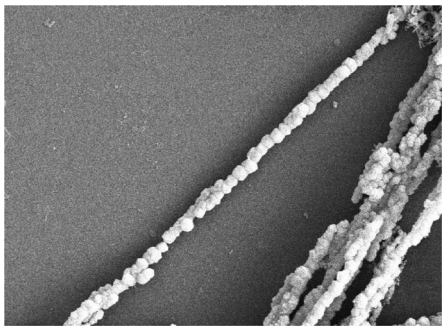

Fe_3O_4 particle-chain microwires are firstly synthesized under magnetic field by a simple coprecipitation method. It was supposed that the magnetic field gradient and the particular growing process of particles are the main factors of the formation of these microwires. Magnetic hysteresis curves of Fe_3O_4 microwires were also measured.

$CeAlO_3$ and $Ce_{1-x}R_xAlO_3$ (R = La, Nd) solid solutions: Crystal structure, thermal expansion and phase transitions

L. Vasylechko, A. Senyshyn, D. Trots, R. Niewa, W. Schnelle and M. Knapp

Page 1277

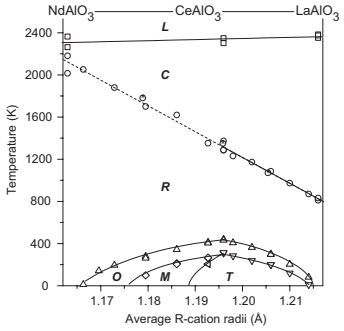

Combined phase diagram of the $CeAlO_3$–$LaAlO_3$ and $CeAlO_3$–$NdAlO_3$ systems, where the transition temperatures are presented as a function of the average radius of rare-earth cations. The letters indicate ***L***iquid, ***C***ubic, ***R***hombohedral, ***O***rthorhombic, ***M***onoclinic and ***T***etragonal phase fields.

Preparation and optical properties of silica@Ag–Cu alloy core-shell composite colloids

Jianhui Zhang, Huaiyong Liu, Zhenlin Wang and Naiben Ming

Page 1291

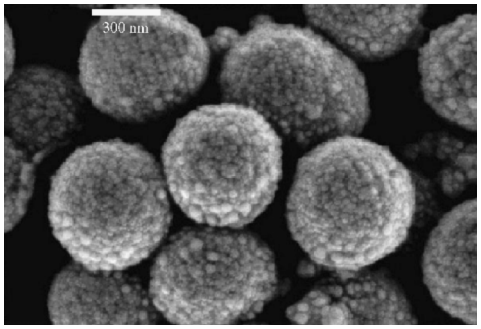

The silica@Ag–Cu alloy core-shell colloids have been successfully synthesized to explore the possibility of modifying the surface plasmon resonance (SPR) by varying the metal nanoshell composition for the first time. Varying the Cu/Ag ratio of the alloy nanoshell has obvious influences on the SPR of the composite colloids and the Raman bands of the amorphous silica core.

Structure and vibrational dynamics of isotopically labeled lithium borohydride using neutron diffraction and spectroscopy

Michael R. Hartman, John J. Rush, Terrence J. Udovic, Robert C. Bowman Jr. and Son-Jong Hwang

Page 1298

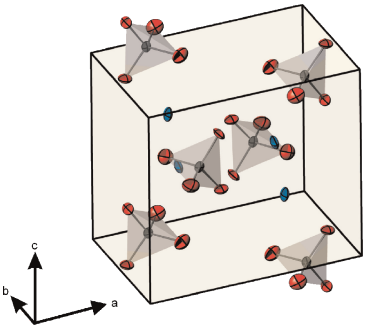

The structure of $^{7}Li^{11}BH_4$ in the low-temperature *Pnma* phase, including atomic displacement ellipsoids, at 3.5 K.

Lithium conductivity in an Li-bearing double-ring silicate mineral, sogdianite

S.-H. Park, M. Hoelzel, H. Boysen and E. Schmidbauer

Page 1306

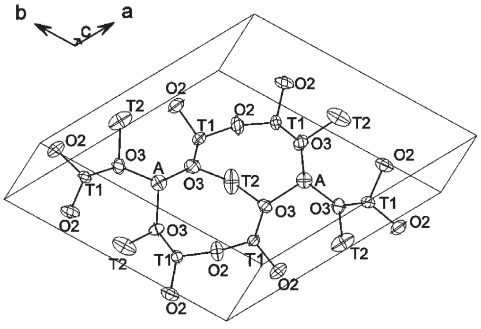

Structure of sogdianite with atomic displacement parameter (ADP) ellipsoids at 1273 K.

A comparative study of the magnetic properties and phase separation behavior of the rare earth cobaltates, $Ln_{0.5}Sr_{0.5}CoO_3$ (Ln = rare earth)

Asish Kundu, R. Sarkar, B. Pahari, A. Ghoshray and C.N.R. Rao

Page 1318

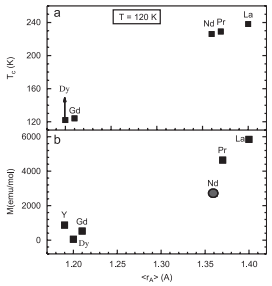

Variation of (a) T_c and (b) FC magnetization at 1000 Oe with $\langle r_A \rangle$ at 120 K in $Ln_{0.5}Sr_{0.5}CoO_3$ and $Dy_{0.34}Nd_{0.16}Sr_{0.40}Ca_{0.10}CoO_3$.

Dependence of nitrogen doping on TiO_2 precursor annealed under NH_3 flow

Xiaoming Fang, Zhengguo Zhang, Qinglin Chen, Hongbing Ji and Xuenong Gao

Page 1325

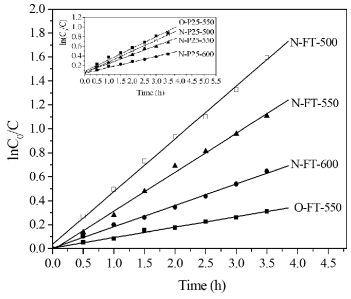

The N-doped TiO_2 powders prepared by annealing the TiO_2 xerogel (named FT) under NH_3/Ar flow exhibited obvious visible-light activities, whereas annealing P25 under the same conditions did not produce the photocatalysts with improved visible-light activities.

Synthesis, structure and properties of $Li_2Rh_3B_2$

Mark S. Bailey, Emil B. Lobkovsky, David G. Hinks, Helmut Claus, Yew San Hor, John A. Schlueter and John F. Mitchell

Page 1333

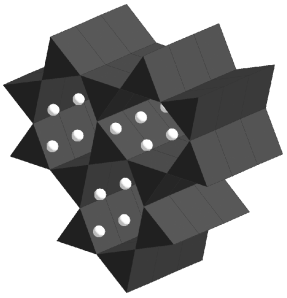

$Li_2Rh_3B_2$, a diamagnetic metal, has been synthesized from a lithium flux. It adopts a distortion of the $CeCo_3B_2$ structure type and is closely related to the 3 K superconductor, $LaRh_3B_2$. Pairs of lithium ions (white) fill the channels formed by rhodium–boron trigonal prisms (gray).

Continued

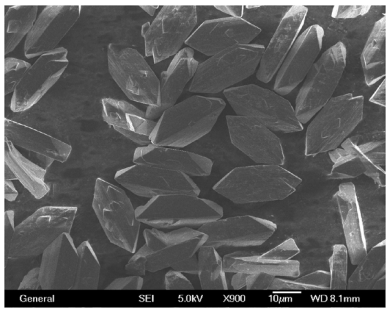

Several RMn_2O_5 (R = La, Pr, Nd, Tb, Bi) and $LaMn_2O_{5+\delta}$ crystallites were prepared by the mild hydrothermal treatment of mixtures of rare-earth oxides, K-birnessite gel and KOH. The magnetic susceptibility measurements show an antiferromagnetic transition in RMn_2O_5 (R = Pr, Nd, Bi). Magnetic susceptibility of the $LaMn_2O_{5+\delta}$ was variable at low temperature due to the different oxygen excess in the compound, which is dominated by the different KOH concentration used in the hydrothermal synthesis.

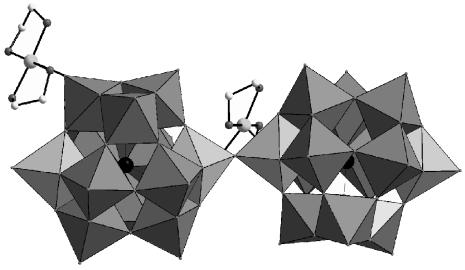

A one-dimensional coordination polymer which represents the first example of 1D organic-inorganic hybrid based on the bimolecular Keggin POMs $\{[Cu(en)_2]_2[Cu_2Si_2W_{22}O_{78}]\}^{8-}$ has been hydrothermally synthesized and characterized.

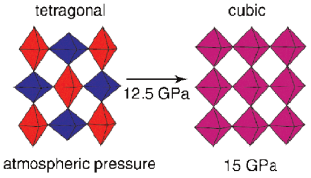

Single-crystal X-ray diffraction study under high pressures up to 18 GPa by using a diamond-anvil-cell with helium gas as an ideal hydrostatic pressure medium has revealed that a perovskite-type gold mixed-valence compound, $Cs_2Au^IAu^{III}Cl_6$, exhibits the structural phase transition from tetragonal to cubic at 12.5 GPa accompanying gold valence transition.

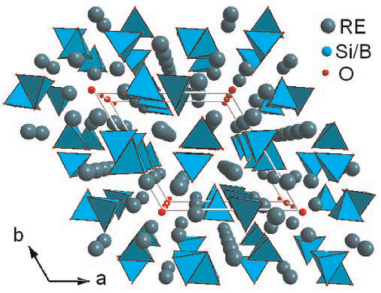

The perspective view of $RE_5Si_2BO_{13}$ (RE = La, Gd, Y) oxyapatite along [001] direction. All non-tetrahedral metal sites are occupied by RE^{3+}, and the tetrahedral sites by SiO_4 and BO_4 groups. $Y_5Si_2BO_{13}$ is a good host for both Eu^{3+} and Tb^{3+} activated phosphors.

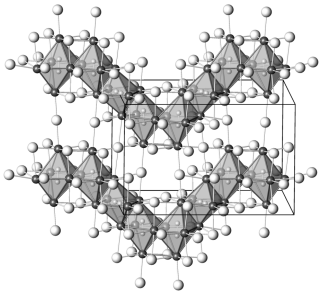

Zigzag chains of edge-sharing metal atom octahedra in $Ln_{12}(C_2)_3I_{17}$.

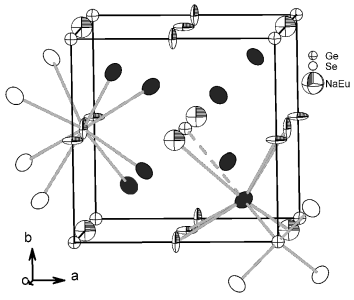

Related quaternary chalcogenides, $Na_2EuGeSe_4$ (**I**) and its ordered superstructure $Na_{0.75}Eu_{1.625}GeSe_4$ (**II**), have been synthesized employing solid-state reactions. The structures of these compounds contain isolated $GeSe_4$ trerahedra and are related to the CsCl-type structure. These compounds are semiconducting with optical band gaps around 2 eV.

Controlled synthesis of CuO nanostructures by a simple solution route

Zeheng Yang, Jun Xu, Weixin Zhang, Anping Liu and Shupei Tang

Page 1390

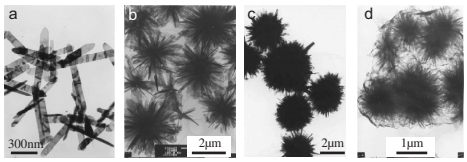

CuO nanorods/nanoribbons and their assemblies into hierarchical structures have been synthesized, respectively, by manipulating reaction conditions in a simple solution route.

On the structural and magnetic properties of the ternary silicides $Ce_6M_{1.67}Si_3$ (M = Co, Ni) and $Ce_5Ni_{1.85}Si_3$

E. Gaudin and B. Chevalier

Page 1397

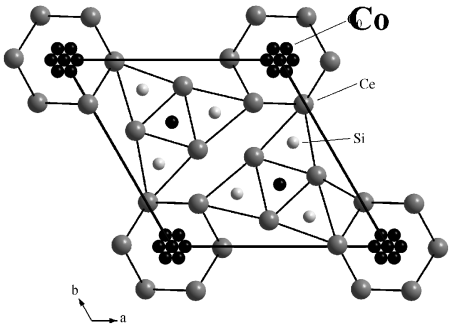

Projection along the c-axis of the structure of $Ce_6Co_{1.67}Si_3$. A strong delocalisation of cobalt atoms is observed in the chains of cerium octahedra.

Blue photoluminescence in Ti-doped alkaline-earth stannates

Takahiro Yamashita and Kazushige Ueda

Page 1410

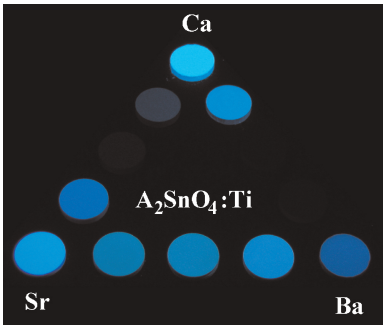

Blue photoluminescence properties of Ti-doped alkaline-earth stannates, $A_2(Sn_{1-x}Ti_x)O_4$ (A = Ca, Sr, Ba) (x = 0.005–0.15), were examined at room temperature. These stannates showed intense broad emission bands peaking at 445 nm for Ca_2SnO_4, at 410 nm for Sr_2SnO_4, and at 425 nm for Ba_2SnO_4 under UV excitation.

High-temperature thermoelectric studies of $A_{11}Sb_{10}$ (A = Yb, Ca)

Shawna R. Brown, Susan M. Kauzlarich, Franck Gascoin and G. Jeffrey Snyder

Page 1414

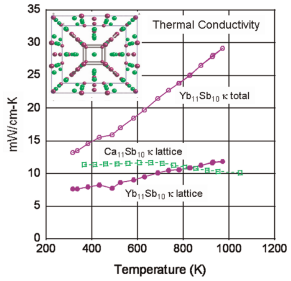

Large samples (6–8 g) of $Yb_{11}Sb_{10}$ and $Ca_{11}Sb_{10}$ have been synthesized from a Sn-flux method. Thermoelectric measurements from room temperature to 1075 K have been obtained. Both $A_{11}Sb_{10}$ (A = Yb, Ca) materials exhibit remarkably low lattice thermal conductivity (~10 mW/cm K for both $Yb_{11}Sb_{10}$ and $Ca_{11}Sb_{10}$) that can be attributed to the complex crystal structure.

Host-sensitized luminescence of Dy^{3+}, Pr^{3+}, Tb^{3+} in polycrystalline $CaIn_2O_4$ for field emission displays

Xiaoming Liu, Ran Pang, Qin Li and Jun Lin

Page 1421

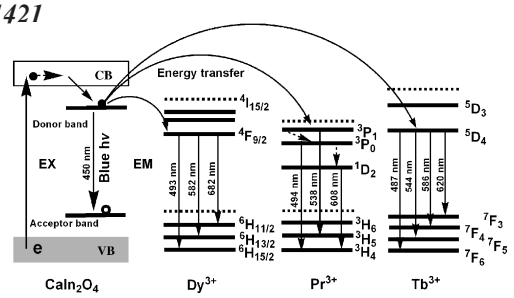

The $CaIn_2O_4$:Dy^{3+}/Pr^{3+}/Tb^{3+} blue–white/green/green phosphors were prepared by the Pechini sol–gel process. Under the excitation of ultraviolet light and low-voltage electron beams (1–5 kV), the $CaIn_2O_4$:Dy^{3+}, $CaIn_2O_4$:Pr^{3+} and $CaIn_2O_4$:Tb^{3+} phosphors show the characteristic emissions of Dy^{3+} ($^4F_{9/2}$–$^6H_{15/2}$ and $^4F_{9/2}$–$^6H_{13/2}$ transitions, blue–white), Pr^{3+} ($^3P_0$–$^3H_4$, $^1D_2$–$^3H_4$ and $^3P_1$–$^3H_5$ transitions, green) and Tb^{3+} ($^5D_4$–$^7F_{6,5,4,3}$ transitions, green), respectively. All the luminescence is resulted from an efficient energy transfer from the $CaIn_2O_4$ host lattice to the doped Dy^{3+}, Pr^{3+} and Tb^{3+} ions.

Nano size crystals of goethite, α-FeOOH: Synthesis and thermal transformation

Axel Nørlund Christensen, Torben R. Jensen, Christian R.H. Bahl and Elaine DiMasi

Page 1431

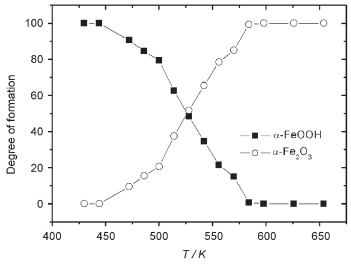

Nano size crystals of goethite, α-FeOOH formed from amorphous iron(III) hydroxide after 23 years, and transforms faster to α-Fe_2O_3 upon heating.

Continued

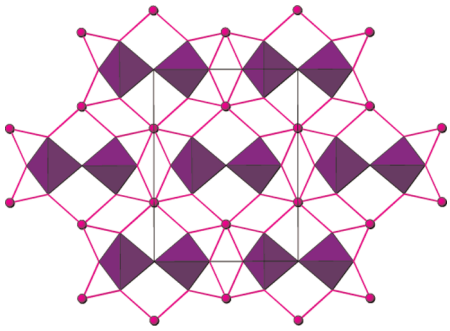

Structural changes with temperature and composition in the $Sc_2Si_2O_7$–$Y_2Si_2O_7$ system are analysed using XRD and ^{29}Si MAS NMR. The temperature–composition diagram is dominated by β-$RE_2Si_2O_7$, with γ-$RE_2Si_2O_7$ and δ-$RE_2Si_2O_7$ showing very reduced stability fields. The analogous $Lu_2Si_2O_7$–$Y_2Si_2O_7$ system shows much wider γ-$RE_2Si_2O_7$ and δ-$RE_2Si_2O_7$ fields, due to the higher radius of Lu^{3+} compared to Sc^{3+}.

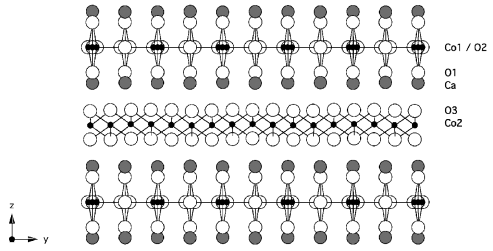

The incommensurately modulated composite structure of $[Ca_2CoO_{2.86}][CoO_2]_{1.61}$.

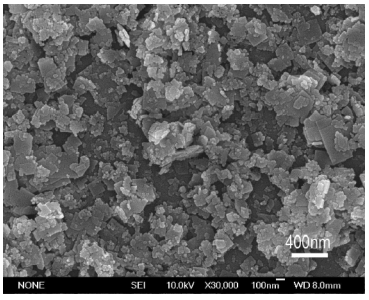

Bi_2WO_6 multilayer film fabricated by layer-by-layer technique.

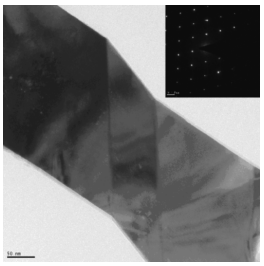

Transmission electron microscopy image of a CuO nanoplatelet. The inset is an electron diffraction pattern of this twined CuO nanoplatelet exhibiting a monoclinic crystal structure.

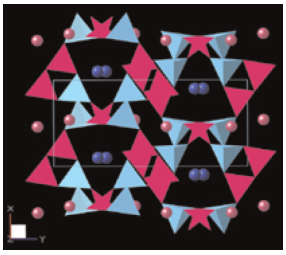

The subsolidus phase relations in the B-rich part of Na_2O–SrO–B_2O_3 system has been investigated by powder diffraction. At the same time, two new pentaborates, $NaSrB_5O_9$ and $Na_3SrB_5O_{10}$, have been successfully synthesized by standard solid-state reaction, and the crystal structure of $NaSrB_5O_9$ has been refined by Rietveld method based on the structural model of $NaCaB_5O_9$. It crystallizes in the monoclinic space group $P2_1/c$ with lattice parameters: $a = 6.4963(1)$ Å, $b = 13.9703(2)$ Å, $c = 8.0515(1)$ Å, $\beta = 106.900(1)^\circ$. The fundamental building units are $[B_5O_9]^{3-}$ anionic groups, and structure is composed of separated [BO] sheets, with Na atoms located in between the sheets and Sr atoms surrounded by the [BO] groups.

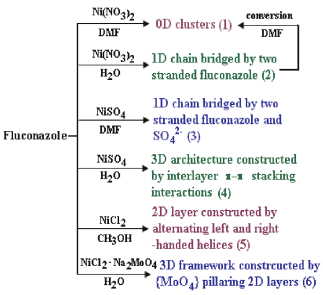

Six novel Ni(II)–fluconazole complexes have been hydro(solvo)thermally synthesized under similar conditions except different anions and solvents. Their structures span zero, one, two and three dimensions. Their different photoluminescence properties indicate that the introduction of different anions to metal–drug complexes can enhance or weaken the intra-ligand transitions of drug.

Oxygen nonstoichiometry and transport properties of strontium substituted lanthanum ferrite
Martin Søgaard, Peter Vang Hendriksen and Mogens Mogensen
Page 1489

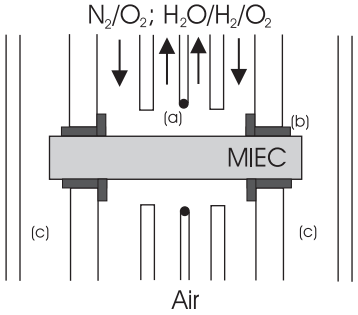

Oxygen permeation measurements are successfully interpreted based on oxygen nonstoichiometry data and determined transport parameters for the perovskite $(La_{0.6}Sr_{0.4})_{0.99}FeO_{3-\delta}$.

The crystal chemistry of $Bi_6TP_2O_{15+x}$, T = Fe, Ni, Zn: Isomorphism and polymorphism, structural relationship to $Bi_6TiP_2O_{16}$
N. Arumugam, V. Lynch and H. Steinfink
Page 1504

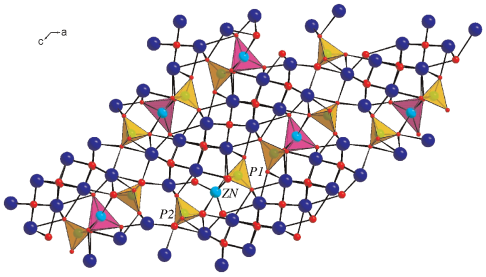

View of the structure of $Bi_6ZnP_2O_{15}$ parallel to the *b*-axis.

Nature of the chemical bond and prediction of radiation tolerance in pyrochlore and defect fluorite compounds
Gregory R. Lumpkin, Miguel Pruneda, Susana Rios, Katherine L. Smith, Kostya Trachenko, Karl R. Whittle and Nestor J. Zaluzec
Page 1512

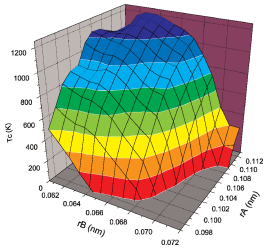

Three-dimensional representation of the predicted critical amorphization temperature in pyrochlores.

Anisotropic thermal expansion and hydrogen bonding behavior of portlandite: A high-temperature neutron diffraction study
H. Xu, Y. Zhao, S.C. Vogel, L.L. Daemen and D.D. Hickmott
Page 1519

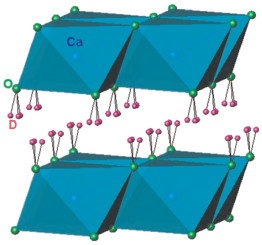

With increasing temperature, the $Ca(OD)_2$ structure expands ~4.5 times larger between the $[CaO_6]$ octahedral layers than within the layers. Correspondingly, the D-mediated interatomic interactions become significantly weakened, and the three equivalent sites over which D is disordered become further apart, suggesting a more delocalized configuration of D at elevated temperatures.

Author inquiries

Submissions

For detailed instructions on the preparation of electronic artwork, consult Elsevier's Author Gateway at http://authors.elsevier.com.

Other inquiries

Visit Elsevier's Author Gateway (http://authors.elsevier.com) for the facility to track accepted articles and set up e-mail alerts to inform you of when an article's status has changed. The Author Gateway also provides detailed artwork guidelines, copyright information, frequently asked questions and more.

Contact details for questions arising after acceptance of an article, especially those relating to proofs, are provided after registration of an article for publication.

Language Polishing

Authors who require information about language editing and copyediting services pre- and post-submission should visit http://www.elsevier.com/wps/find/authorshome.authors/languagepolishing or contact authorsupport@elsevier.com for more information. Please note Elsevier neither endorses nor takes responsibility for any products, goods, or services offered by outside vendors through our services or in any advertising. For more information please refer to our Terms & Conditions at http://www.elsevier.com/wps/find/termsconditions.cws_home/termsconditions.

For a full and complete Guide for Authors, please refer to *J. Solid State Chem.*, Vol. 180, Issue 1, pp. *bmi–bmv*. The instructions can also be found at http://www.elsevier.com/wps/find/journaldescription.cws_home/622898/authorinstructions.

Journal of Solid State Chemistry has no page charges.